Catalysis Science & Technology

ROYAL SOCIETY OF CHEMISTRY

PAPER

View Article Online
View Journal | View Issue



Cite this: *Catal. Sci. Technol.*, 2026, **16**, 2139

# Facile synthesis of metal-free N-doped carbon electrocatalyst from acetone aldol reaction products towards selective $CO_2$-to-CO conversion

Kou Adachi,[a] Ryuji Takada,*[a] Koji Miyake, *[ab] Yoshiaki Uchida [a] and Norikazu Nishiyama[ab]

Received 5th December 2025,
Accepted 28th January 2026

DOI: 10.1039/d5cy01484k

rsc.li/catalysis

Electrochemical $CO_2$ reduction ($CO_2$RR) is a promising method for producing useful chemicals from $CO_2$ using electricity, including that derived from renewable energy sources. Among the possible products, CO is an important intermediate in the synthesis of fuels and chemicals. Metal-free carbon catalysts have been proposed as durable and low-cost alternatives to metal-based catalysts. However, many synthesis routes involve complex steps or the use of transition metals. In this study, we propose a simple method for preparing a metal-free catalyst using acetone aldol reaction products and ammonium chloride. This catalyst achieved a CO Faradaic efficiency of 87.9% at −0.6 V *vs.* RHE. A structure–activity analysis revealed that the CO current density showed a positive correlation with specific surface area and an inverse correlation with total nitrogen content. This finding indicates that nitrogen desorption contributes to the formation of abundant pores. This enhanced porous structure is expected to improve mass transport and active site exposure, thereby enhancing catalytic performance.



## Introduction

In recent years, electrochemical reduction of carbon dioxide ($CO_2$RR) has attracted attention as a means to mitigate global warming and support a sustainable society. This process uses electricity from renewable sources to convert $CO_2$ into useful chemicals. Among the possible products, CO is an important material because it can be used as an intermediate to produce many valuable chemicals, such as methanol, acetic acid, and synthetic fuels.[1–3] To drive $CO_2$RR efficiently, metal catalysts such as Au,[4] Ag,[5] and Zn[6] have been studied. However, they have limitations such as high cost and poor durability due to metal dissolution or structural changes during reaction.[7] Therefore, it is necessary to design durable, cost-effective alternatives to metal catalysts for $CO_2$RR.

In this context, metal-free N-doped carbon materials have emerged as promising candidates for $CO_2$RR electrocatalysts owing to their low cost[2] and good durability.[8] To date, various N-doped carbon catalysts, including N-doped graphene,[9] carbon nanotubes,[10] nanodiamond,[11] ordered porous carbon,[12] carbon fibers[13] and MOF-derived carbon[14] have been explored. To achieve high catalytic performance, research has largely focused on regulating nitrogen species, which are considered to generate active sites, and on engineering the porous structure.[15] As for N species, while pyridinic N has conventionally been considered the principal active site,[16] more recent investigations suggest that carbon atoms next to graphitic N domains may function as the active sites.[17] Moreover, recent studies have shown that although the intrinsic activity of pyrrolic-N is sufficiently high, its activity is suppressed by interactions with neighboring pyridinic N.[18] Meanwhile, it has also been reported that increasing the overall N doping amount does not necessarily enhance catalytic activity,[19] indicating that a definitive understanding of the active sites remains unresolved. Regarding the pore structure, a hierarchical porous structure is considered to enhance catalytic activity. Such a morphology combines micropores, which increase $CO_2$ adsorption and local $CO_2$ concentration, with meso- and macropores that promote efficient mass transport.[20–22]

However, many of them require complicated synthetic methods,[23,24] expensive precursors,[25] or specialized equipment[13,26] to achieve high catalytic performance. For instance, the synthesis of ordered porous carbon *via* the hard-template method requires the removal of the template using an acid or base solution.[27] Likewise, the preparation of carbons derived from metal–organic frameworks (MOFs), such as ZIF-8, also requires a washing process.[28] Moreover, a more significant issue arises with MOF-derived carbons; the precursors contain transition metals (*e.g.*, Zn in ZIF-8) that are themselves known

[a] *Division of Chemical Engineering, Graduate School of Engineering Science, The University of Osaka, 1-3 Machikaneyama, Toyonaka, Osaka 560-8531, Japan. E-mail: r.takada@cheng.es.osaka-u.ac.jp, kojimiyake@cheng.es.osaka-u.ac.jp*
[b] *Innovative Catalysis Science Division, Institute for Open and Transdisciplinary Research Initiatives (ICS-OTRI), The University of Osaka, Suita 565-0871, Japan*

to be active for $CO_2$RR. Indeed, the high-temperature pyrolysis of such MOFs is a prominent strategy for synthesizing single-atom catalysts (SACs),[29] in which isolated Zn atoms coordinated to nitrogen (forming Zn–N–C sites) serve as an active site.[30] This presents a fundamental challenge because it is difficult to determine whether the observed catalytic activity arises from the N-doped carbon framework itself or from the highly active, residual Zn–N–C sites. Hence, it is important to develop a synthetic method for high-performance catalysts that is both facile and strictly transition-metal-free.

In this study, we report a facile synthesis of an N-doped carbon electrocatalyst using the products of an acetone aldol reaction as the carbon precursor and ammonium chloride as the nitrogen source. This catalyst achieved a CO Faradaic efficiency of 87.9% at −0.6 V *vs.* RHE, despite being synthesized using a simple method that avoids transition metals, expensive precursors, and complicated steps.

# Experimental

### Materials

Sodium hydroxide (NaOH), acetone, ammonium chloride ($NH_4Cl$) and Nafion (5 wt%) were obtained from Wako Pure Chemical Industries.

### Preparation of N-doped carbons (CN-*T*)

Acetone (20 mL) and NaOH (4.0 g) were mixed and stirred at 1500 rpm for 1 hour at room temperature. After mixing, the solution was maintained at room temperature for 3 days under ambient conditions to yield the carbon precursor.[31] The precursor (300 mg) was mixed with $NH_4Cl$ (300 mg). The mixture was pyrolyzed at $T$ °C ($T$ = 900, 1000, 1100, 1200) for 3 hours under $N_2$ flow. The catalysts were named "CN-$T$". For comparison, C-1000 was prepared by pyrolyzing the precursor (300 mg) alone at 1000 °C under the same conditions. The yields are shown in Table. S1.

### Preparation of N-doped carbons (CN-*x*)

The carbon precursor was prepared using the procedure described above. The precursor (300 mg) was then mixed with various amounts of $NH_4Cl$ (150, 300, 600, or 900 mg). Each mixture was pyrolyzed at 1000 °C for 3 hours under $N_2$ flow. Catalysts were named "CN-$x$", where $x$ (0.5, 1, 2, or 3) represents the mass ratio of the $NH_4Cl$ dopant to the carbon precursor. The yields are shown in Table. S1.

### Characterizations

Transmission electron microscope (TEM) was carried out using an H800 (Hitachi, Japan). X-ray diffraction (XRD) was conducted on a PANalytical X'Pert-MDR diffractometer using Cu Kα radiation. $N_2$ adsorption isotherms at 77 K were recorded using a BELSORP MINI X (Microtrac MRB, Japan). Pore volumes, pore size distributions, and the specific surface areas were determined based on the BJH (Barrett–Joyner–Halenda) and Brunauer–Emmett–Teller (BET) methods. Analysis for C, H and N contents was conducted using FlashEA (Thermo Fisher Scientific, USA). X-ray photoelectron spectroscopy (XPS) was conducted using a Kratos Ultra 2 (Shimadzu, Japan). Raman spectra of samples were recorded using a confocal Raman microscope (LabRAM HR-800, Horiba, Ltd., Kyoto, Japan).

### Electrochemical measurements

Isopropanol, nafion (5 wt% in alcohol and water) and water were mixed in a volume ratio of 1 : 1 : 8. A catalyst (5 mg) was suspended in the solution (500 μL), and the suspension was ultrasonicated to obtain the catalyst ink. The ink (100 μL) was pipetted on a carbon paper. The mass loading of a catalyst on the carbon paper was fixed at 1 mg $cm^{-2}$. A Biologic SP-50e potentiostat (TOYO, Japan) was used as an electrochemical analyzer. An as-prepared working electrode, Ag/AgCl (reference electrode), and a platinum wire (counter electrode) were equipped in a H-type cell. The potentials in this study were relative to the reversible hydrogen electrode (RHE), based on the following equation:

$$E_{RHE} = E_{Ag/AgCl} + 0.208 + 0.0591 \times pH$$

Linear sweep voltametric (LSV) measurements with a scan rate of 5 mV $s^{-1}$ were performed in $CO_2$-saturated and $N_2$-saturated 0.1 M $KHCO_3$ solution, and the potential range was from 0.15 V to −1.2 V *vs.* RHE. During the LSV measurements, $CO_2$ and $N_2$ keep flowing. $CO_2$ splitting experiments were carried out in a $CO_2$-saturated 0.1 M $KHCO_3$ solution with stirring at 350 rpm. Before $CO_2$ splitting experiments, the 0.1 M $KHCO_3$ solution was pre-saturated with $CO_2$ for at least 30 minutes. The gas-phase products were quantified by offline gas chromatography (GC) (GC-8A, Shimadzu, Japan) using a Shincarbon-ST column (SHINWA, Japan). The products in a liquid phase were detected using an $^1$H NMR (ECS, JEOL, Japan). The below equations were applied to calculate the faradaic efficiencies of the gas products:

$$FE = \frac{\text{moles of products}}{Q/nF} \times 100\%$$

FE (%) = faradaic efficiency;

$Q$ (C) = electric quantity;

$n$ (−) = electron transfer number;

F (C $mol^{-1}$) = Faraday constant, 96 485.33 C $mol^{-1}$

$$* + CO_2(g) + H^+ + e^- \rightarrow COOH*$$

$$COOH* + H^+ + e^- \rightarrow CO* + H_2O(l)$$

$$CO* \rightarrow * + CO(g)$$

Electrochemical impedance spectroscopy (EIS) measurements were conducted in a $CO_2$-saturated $KHCO_3$ solution at a half cell. The frequency limits were set in the range from 0.1 Hz to 200 kHz with a voltage amplitude of 10 mV.

## Results & discussion

Preparation of the carbon precursor *via* the aldol reaction of acetone. The aldol reaction of acetone was catalyzed by NaOH, resulting in the formation of a reddish-brown liquid within 30 minutes. This solution was then left for 3 days at room temperature and ambient pressure, during which it solidified to yield the final blackish-brown carbon precursor (photographs in Fig. S1 and XPS spectra in Fig. S2). To prepare the N-doped carbon catalysts, a mixture of the precursor and $NH_4Cl$ was calcined under flowing $N_2$.

As revealed in the XRD patterns (Fig. S3(a)), a clear structural difference was observed depending on the carbonization temperature. The pattern for CN-900 showed distinct peaks attributed to crystalline sodium salts.[32,33] In contrast, the salt peaks disappeared for CN-1000, CN-1100, and CN-1200. Instead, the appearance of two broad peaks at approximately 25° and 44°—belonging to the (002) and (101) planes of graphitic carbon[34]—indicates the successful conversion of the precursor into carbon. These findings are strongly corroborated by the Na 1s XPS spectra (Fig. S3(b)). A clear signal was observed for CN-900, while no peaks were present for CN-1000, CN-1100, and CN-1200. Therefore, the absence of Na-based impurities in both the XRD patterns and XPS Na 1s spectra of the samples prepared at 1000 °C and above suggests the evaporation of Na species from the surface during the high-temperature annealing process. To further confirm this removal, thermogravimetric analysis (TGA) of CN-900 and CN-1000 was performed under an air flow (Fig. S3(c)). For CN-900, a sharp weight loss was observed at approximately 880 °C, corresponding to the boiling point of sodium, whereas CN-1000 showed no change in weight. This result confirms that the Na species were completely removed from the surface and the bulk of the catalyst.

The morphologies of the precursor and catalysts were characterized using TEM. The precursor (Fig. 1(a)) was found to be unstable under the electron beam, which prevented clear imaging of its structure. In contrast, the final catalyst, CN-*T* (Fig. 1(b)–(d)), exhibited a sheet-like morphology. Additionally, crystal-like structures were visible, which were presumed to be imprints left by the removal of the sodium salt derived from the NaOH added as a catalyst for the aldol reaction. $N_2$ adsorption–desorption measurements (Fig. S4) revealed that the specific surface area decreased as the carbonization temperature increased, and the catalyst possessed a porous structure composed of micropores and macropores. Raman spectroscopy analysis (Fig. S5) confirmed the presence of a D band (~1370 $cm^{-1}$) and a G band (~1600 $cm^{-1}$) for all the catalysts. No significant differences were observed in the $I_D/I_G$ ratios among the various samples.

Electrochemical measurements were used to evaluate the electrocatalytic performance of the $CO_2RR$ in an H-type cell. LSV measurements were conducted in both $N_2$-saturated and $CO_2$-saturated 0.1 M $KHCO_3$ solution using C-1000 and CN-1000 (Fig. S6). For C-1000, no significant difference in current density was observed between the two atmospheres. CN-1000 exhibited a higher current density in $CO_2$-saturated 0.1 M $KHCO_3$ solution than in $N_2$-saturated 0.1 M $KHCO_3$ solution at a positive potential of −1 V *vs.* RHE, suggesting a high catalytic activity for $CO_2RR$.

Furthermore, the selectivity of electroreduction products for CN-1000 and C-1000 at various potentials was investigated using a controlled potential electrolysis method (Fig. 2(a)–(d)). The measurement was conducted at potentials in 0.1 V increments from −0.5 to −0.8 V *vs.* RHE for 1.5 h. The products in the liquid phase obtained from the experiment were investigated using $^1H$ NMR, but they were below the detection limit. The electroreduction products were confirmed to be only gas-phase products. Products in the gas phase, mainly CO and $H_2$, were yielded within the potential window from −0.5 V to −0.8 V *vs.* RHE. The CN-1000 catalyst exhibited the highest $FE_{CO}$ of 87.9% and $j_{CO}$ of 0.25 mA $cm^{-2}$ at −0.6 V *vs.* RHE. This activity is comparable to those reported for recently developed metal-free catalysts (Table S2). A decreasing trend in $FE_{CO}$ was observed as the potential shifted more negatively, stemming from the

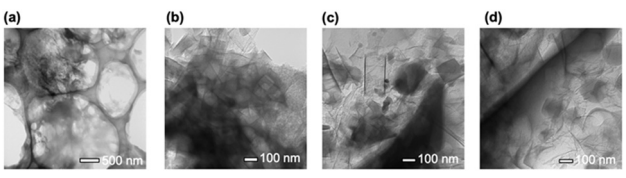


Fig. 1 TEM image of (a) precursor, (b) CN-1000, (c) CN-1100 and (d) CN-1200.

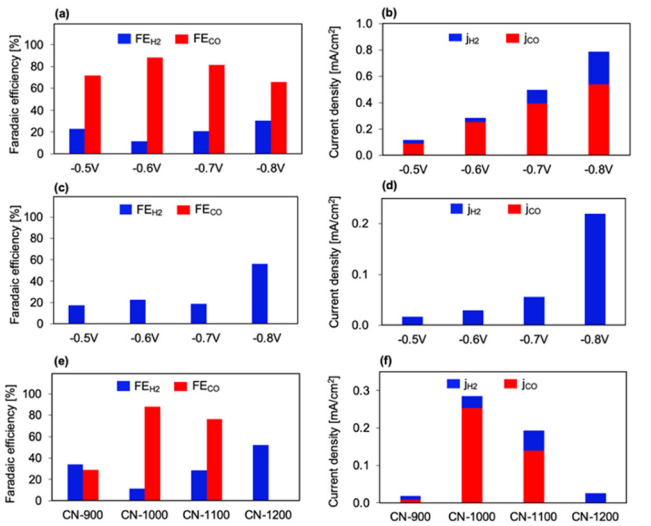


Fig. 2 (a) Faradaic efficiencies of CO and $H_2$ using CN-1000 within the potential window from −0.5 V to −0.8 V *vs.* RHE in $CO_2$-saturated 0.1 M $KHCO_3$ solution, (b) the comparison of partial current density of CO and $H_2$ using CN-1000, (c) faradaic efficiencies of CO and $H_2$ using C-1000 within the potential window from −0.5 V to −0.8 V *vs.* RHE in $CO_2$-saturated 0.1 M $KHCO_3$ solution, (d) the comparison of partial current density of CO and $H_2$ using C-1000, (e) faradaic efficiencies of CO and $H_2$ using CN-*T* within the potential window at −0.6 V *vs.* RHE in $CO_2$-saturated 0.1 M $KHCO_3$ solution and (f) the comparison of partial current density of CO and $H_2$ using CN-*T*.

dominance of the $H_2$ evolution reaction over the $CO_2$RR. For comparison, the $CO_2$RR activity of the C-1000 was also measured under similar conditions. Only $H_2$ was produced during the $CO_2$RR of C-1000. These results demonstrate the positive role of N in improving both the productivity and selectivity in $CO_2$RR. To confirm the carbon source of products by $CO_2$RR, the electrolysis experiment was carried out on CN-1000 in $N_2$-saturated electrolyte at −0.6 V *vs.* RHE (Fig. S7). Only $H_2$ was detected, suggesting that the $CO_2$ gas dissolved in the electrolyte was the only carbon source for producing CO.

Besides the selectivity of electroreduction products, the durability of the $CO_2$RR catalysts is a crucial parameter for practical applications. Chronoamperometric measurement was performed on CN-1000 at −0.6 V *vs.* RHE for 12 h (Fig. S8). The current density slightly declined under continuous operation for up to 12 h because of catalyst stripping from the carbon paper and coating of the catalyst surface with gaseous products. Meanwhile, no decay of $FE_{CO}$ was identified after continuous test for 12 h. The XPS spectra of CN-1000 after the long-term test showed no obvious changes in the bonding states (Fig. S9). These results suggest that the CN-1000 is a stable electrocatalyst for $CO_2$RR.

To gain more insight into the mechanism of the $CO_2$RR performance, the selectivity of electroreduction products for CN-*T* at −0.6 V *vs.* RHE for 1.5 h was investigated (Fig. 2(e) and (f)). The catalyst CN-900, which contained residual sodium, exhibited low activity. This result indicates that the presence of sodium species within the catalyst does not generate activity for the $CO_2$RR. While CN-1000 showed the highest $FE_{CO}$, the activity declined for CN-1100, and was nearly extinguished for CN-1200.

CHN analysis was conducted to determine the total N content in the different CN-*T*, while X-ray photoelectron spectroscopy (XPS) was performed to investigate the chemical states of the doped N. CHN analysis (Table S3) revealed that the total nitrogen content decreased with increasing carbonization temperature. As shown in the N 1s XPS spectra (Fig. 3(a)), all the samples show five types of nitrogen species: pyridinic N (398.2 eV), pyrrolic/pyridonic N (399.8 eV), graphitic N (401.1 eV), and oxidized N (402.8 eV).[35,36] Although similar amounts of $NH_4Cl$ were used, the N distribution of the samples greatly depended on the carbonization conditions (Fig. 3(b)). As the carbonization temperature increased, the rate of pyridinic N decreased, while the rate of pyrrolic N and graphitic N slightly

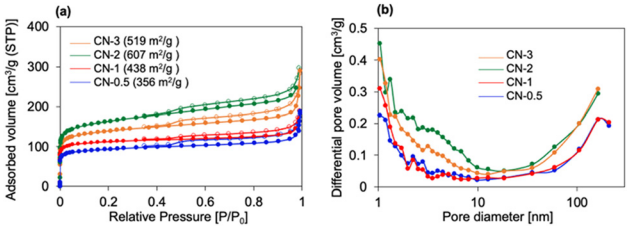


Fig. 4 (a) $N_2$ adsorption–desorption isotherms and (b) pore size distributions of CN-*x*.

increased. The electrochemical measurements and the N-species analysis suggest that the high activity of CN-1000 can be attributed to either a high total nitrogen content, regardless of the specific N species, or a large proportion of pyridinic N.

Next, the CN-*x* series, which was prepared by varying the amount of added ammonium chloride, was examined. All the catalysts in the CN-*x* series exhibited a sheet-like morphology (Fig. S10). A clear difference in porosity was visible in the TEM images. The CN-2 sample exhibited a well-developed porous structure (Fig. S10(c)), while significantly fewer pores were seen in CN-0.5 (Fig. S10(a)). These visual observations are consistent with the $N_2$ adsorption–desorption measurements (Fig. 4(a) and (b)), indicating that CN-2 possessed the highest specific surface area and CN-0.5 had the lowest. In the Raman spectroscopy analysis (Fig. S11), no significant difference was observed in the $I_D/I_G$ ratios among the various samples.

An analysis of the nitrogen species was conducted. The CHN analysis (Table S4) revealed an unexpected trend for the total N content. It was not proportional to the amount of added ammonium chloride. Instead, CN-2 exhibited the lowest N content, while CN-0.5 showed the highest. In contrast, XPS measurements (Fig. 5(a) and (b)) indicated that the ratio of the N species was nearly identical across the different catalysts.

The selectivity of electroreduction products for CN-*x* from −0.5 V to −0.8 V *vs.* RHE for 1.5 h was investigated. The results for −0.6 V are presented in the main text (Fig. 6), while the data for the other potentials (−0.5 V, −0.7 V, and −0.8 V) are compiled in the Supporting Information (Fig. S12). In terms of $FE_{CO}$, a notable difference was observed. While CN-1, CN-2, and CN-3 achieved similarly high values, the performance of CN-0.5 was lower (Fig. 6(a)). Regarding the current density, the activity peaked at CN-2, which exhibited

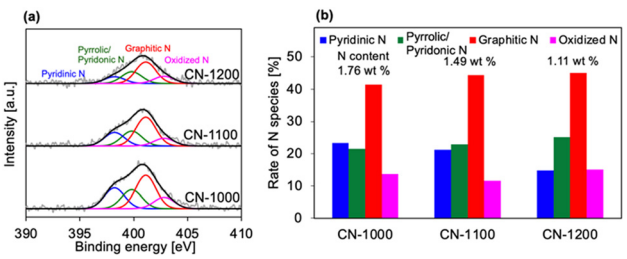


Fig. 3 (a) The N 1s XPS spectra of CN-*T* and (b) the rate of N species in CN-*T*.

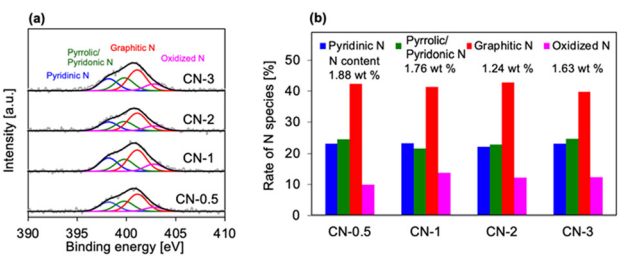


Fig. 5 (a) The N 1s XPS spectra of CN-*x* and (b) the rate of N species in CN-*x*.

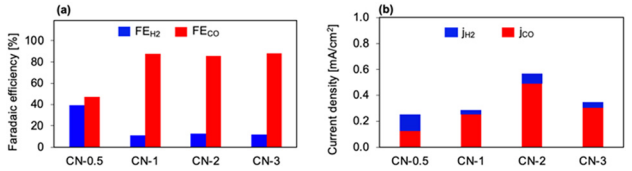


Fig. 6 (a) Faradaic efficiencies of CO and $H_2$ using CN-*x* with the potential window at −0.6 V *vs.* RHE in $CO_2$-saturated 0.1 M $KHCO_3$ solution, (b) the comparison of partial current density of CO and $H_2$ using CN-*x*.

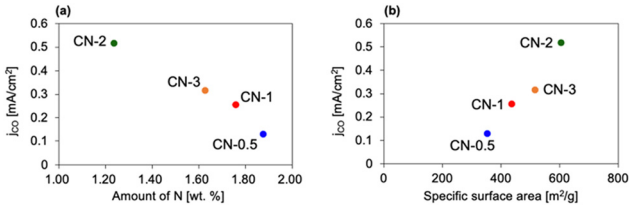


Fig. 7 (a) Plot of $j_{CO}$ as a function of the total N content and (b) plot of $j_{CO}$ as a function of the specific surface area.

the highest current density ($j_{CO}$ = 0.49 mA cm$^{-2}$.), and then decreased for catalysts with both lower and higher dopant ratios (Fig. 6(b)). The superior activity of CN-2 is supported by EIS (Fig. S13), which reveals that CN-2 possesses the highest conductivity. When measured at −0.4 V *vs.* RHE in $CO_2$-saturated $KHCO_3$, CN-2 displayed the smallest charge transfer resistance, suggesting that its enhanced performance is due to faster reaction kinetics.

The characterization data provides insight into the structure–activity relationships of the catalysts. First, the relationship between the total N content and the partial current density for CO production ($j_{CO}$) was examined. A clear inverse correlation was observed (Fig. 7(a)). Catalysts with lower nitrogen content consistently exhibited higher $j_{CO}$ values. Subsequently, $j_{CO}$ was plotted against the specific surface area (Fig. 7(b)), revealing a positive linear relationship where a larger surface area leads to higher current density. Taken together, these correlations suggest a plausible mechanism. The thermal desorption of nitrogen species during pyrolysis is believed to generate a rich porous structure. This enhanced porosity likely improves the mass transport of $CO_2$ and CO and increases the exposure of active sites, thereby allowing more sites to function effectively and boosting the overall current density.

## Conclusions

In summary, this study has successfully demonstrated a facile, low-cost, and transition-metal-free synthesis of a high-performance N-doped carbon electrocatalyst from the products of an acetone aldol reaction. The optimized catalyst, CN-1000, exhibited excellent selectivity for the electrochemical conversion of $CO_2$ to CO, achieving a Faradaic efficiency of 87.9%. Our investigation into the structure–activity relationship revealed two key trends. The catalytic current density was inversely proportional to the total nitrogen content but directly proportional to the specific surface area. These findings suggest a mechanism wherein the thermal desorption of nitrogen species during high-temperature pyrolysis is crucial for creating a rich porous architecture. This enhanced porosity, in turn, improves mass transport and active site accessibility, ultimately boosting the catalytic performance. This work not only presents a simple route to an effective catalyst but also provides valuable insights into tuning the structure of carbon-based materials for $CO_2$ reduction.

## Author contributions

Kou Adachi: conceptualization, investigation, visualization, writing – original draft. Ryuji Takada: investigation, visualization, methodology, writing – review & editing. Koji Miyake: conceptualization, supervision, visualization, methodology, writing – review & editing. Yoshiaki Uchida: writing – review & editing. Norikazu Nishiyama: supervision, resources, writing – review & editing.

## Conflicts of interest

There are no conflicts to declare.

## Data availability

The data supporting this article have been included as part of the supplementary information (SI).

Supplementary information: the SI includes photographs of precursor synthesis, XPS (C 1s, O 1s, and Na 1s spectra), XRD patterns, TG curves, $N_2$ adsorption–desorption isotherms, Raman spectra, CHN analysis results, TEM images, LSV curves, Faradaic efficiency results, stability tests, Nyquist plots, and a comparison table of catalytic performance. See DOI: https://doi.org/10.1039/d5cy01484k.

## Acknowledgements

The study was partially conducted using a facility at the Research Center for Ultra-High Voltage Electron Microscopy, Osaka University, Suita, Japan.

## References

1 Y. Hori, in *Modern Aspects of Electrochemistry*, ed. C. G. Vayenas, R. E. White and M. E. Gamboa-Aldeco, Springer, New York, NY, 2008, pp. 89–189.
2 J. Qiao, Y. Liu, F. Hong and J. Zhang, *Chem. Soc. Rev.*, 2013, **43**, 631–675.
3 H.-R. "Molly" Jhong, S. Ma and P. J. Kenis, *Curr. Opin. Chem. Eng.*, 2013, **2**, 191–199.
4 Y. Chen, C. W. Li and M. W. Kanan, *J. Am. Chem. Soc.*, 2012, **134**, 19969–19972.
5 S. Liu, H. Tao, L. Zeng, Q. Liu, Z. Xu, Q. Liu and J.-L. Luo, *J. Am. Chem. Soc.*, 2017, **139**, 2160–2163.

6 L. Gao, S. Bai, Y. Zhang and C. Hu, *ChemCatChem*, 2022, **14**, e202200383.
7 S. Popović, M. Smiljanić, P. Jovanovič, J. Vavra, R. Buonsanti and N. Hodnik, *Angew. Chem., Int. Ed.*, 2020, **59**, 14736–14746.
8 I. Masood ul Hasan, L. Peng, J. Mao, R. He, Y. Wang, J. Fu, N. Xu and J. Qiao, *Carbon Energy*, 2021, **3**, 24–49.
9 J. Wu, M. Liu, P. P. Sharma, R. M. Yadav, L. Ma, Y. Yang, X. Zou, X.-D. Zhou, R. Vajtai, B. I. Yakobson, J. Lou and P. M. Ajayan, *Nano Lett.*, 2016, **16**, 466–470.
10 J. Wu, R. M. Yadav, M. Liu, P. P. Sharma, C. S. Tiwary, L. Ma, X. Zou, X.-D. Zhou, B. I. Yakobson, J. Lou and P. M. Ajayan, *ACS Nano*, 2015, **9**, 5364–5371.
11 Y. Liu, S. Chen, X. Quan and H. Yu, *J. Am. Chem. Soc.*, 2015, **137**, 11631–11636.
12 M. Dai, J. Zeng, K. Luo, W. Zhang, Z. Chen, Z. Zeng, P. Yuan, Y. Zhang, S. Zhang and W. Ni, *ACS Appl. Energy Mater.*, 2025, **8**(8), 5166–5173.
13 H. Yang, Y. Wu, Q. Lin, L. Fan, X. Chai, Q. Zhang, J. Liu, C. He and Z. Lin, *Am. Ethnol.*, 2018, **130**, 15702–15706.
14 J. Li, H. Luo, B. Li, J.-G. Ma and P. Cheng, *Mater. Chem. Front.*, 2023, **7**, 6107–6129.
15 I. Masood ul Hasan, L. Peng, J. Mao, R. He, Y. Wang, J. Fu, N. Xu and J. Qiao, *Carbon Energy*, 2021, **3**, 24–49.
16 S. Liu, H. Yang, X. Huang, L. Liu, W. Cai, J. Gao, X. Li, T. Zhang, Y. Huang and B. Liu, *Adv. Funct. Mater.*, 2018, **28**, 1800499.
17 J. Li, W.-Y. Zan, H. Kang, Z. Dong, X. Zhang, Y. Lin, Y.-W. Mu, F. Zhang, X.-M. Zhang and J. Gu, *Appl. Catal., B*, 2021, **298**, 120510.
18 Y. Shang, Y. Ding, P. Zhang, M. Wang, Y. Jia, Y. Xu, Y. Li, K. Fan and L. Sun, *Chin. J. Catal.*, 2022, **43**, 2405–2413.
19 S. Fu, M. Li, W. de Jong and R. Kortlever, *ACS Catal.*, 2023, **13**, 10309–10323.
20 B. Zhang, J. Zhang, F. Zhang, L. Zheng, G. Mo, B. Han and G. Yang, *Adv. Funct. Mater.*, 2020, **30**, 1906194.
21 U. Karatayeva, S. A. Al Siyabi, B. Brahma Narzary, B. C. Baker and C. F. J. Faul, *Adv. Sci.*, 2024, **11**, 2308228.
22 H. Wang, G. Wang, L. Hu, B. Ge, X. Yu and J. Deng, *Materials*, 2023, **16**, 1630.
23 X. Hao, X. An, A. M. Patil, P. Wang, X. Ma, X. Du, X. Hao, A. Abudula and G. Guan, *ACS Appl. Mater. Interfaces*, 2021, **13**, 3738–3747.
24 Y. Zhu, K. Lv, X. Wang, H. Yang, G. Xiao and Y. Zhu, *J. Mater. Chem. A*, 2019, **7**, 14895–14903.
25 Z. Zhang, L. Yu, Y. Tu, R. Chen, L. Wu, J. Zhu and D. Deng, *Cell Rep. Phys. Sci.*, 2020, **1**, 100145.
26 Y. Ji, Y. Shi, C. Liu and B. Zhang, *Sci. China Mater.*, 2020, **63**, 2351–2357.
27 D. Hursán, M. Ábel, K. Baán, E. Fako, G. F. Samu, H. C. Nguyën, N. López, P. Atanassov, Z. Kónya, A. Sápi and C. Janáky, *ACS Catal.*, 2022, **12**, 10127–10140.
28 B. Pan, X. Zhu, Y. Wu, T. Liu, X. Bi, K. Feng, N. Han, J. Zhong, J. Lu, Y. Li and Y. Li, *Adv. Sci.*, 2020, **7**, 2001002.
29 M. Xie, J. Wang, X.-L. Du, N. Gao, T. Liu, Z. Li, G. Xiao, T. Li and J.-Q. Wang, *RSC Adv.*, 2022, **12**, 32518–32525.
30 F. Yang, P. Song, X. Liu, B. Mei, W. Xing, Z. Jiang, L. Gu and W. Xu, *Angew. Chem.*, 2018, **130**, 12483–12487.
31 H. Hou, C. E. Banks, M. Jing, Y. Zhang and X. Ji, *Adv. Mater.*, 2015, **27**, 7861–7866.
32 M. H. Masood, N. Haleem, I. Shakeel and Y. Jamal, *Res. Chem. Intermed.*, 2020, **46**, 5165–5180.
33 A. Harabor, P. Rotaru and N. A. Harabor, *Ann. Univ. Craiova, Phys. AUC.*, 2013, **23**, 79–88.
34 P. Pachfule, B. P. Biswal and R. Banerjee, *Chem. – Eur. J.*, 2012, **18**, 11399–11408.
35 S. Gupta and N. Dimakis, *J. Appl. Phys.*, 2021, **130**, 084902.
36 Y. Wen, T. E. Rufford, D. Hulicova-Jurcakova and L. Wang, *ChemSusChem*, 2016, **9**, 513–520.

 